

Design, Construction, and Performance Testing of a 6.5 T Superconducting Wavelength Shifter

C. S. Hwang, B. Wang, B. Wahrer, C. Taylor, C. Chen, T. Juang, F. Y. Lin, J. C. Jan, C. H. Chang, H. H. Chen, M. H. Huang, K. T. Hsu, and G. Y. Hsiung

Abstract—A compact three-pole superconducting magnet with an aluminum warm beam duct was designed and fabricated as an X-ray source in a 1.5 GeV Taiwan Light Source (TLS) or the 3 GeV Taiwan Photon Source (TPS). Three pairs of racetrack NbTi superconducting coils were connected to one main power supply to create a central field of over 6.5 T. Two low current trim power supplies were connected in parallel to the two side pairs of the coil to eliminate the first and second field integrals. The wavelength shifter magnet was cooled in a pool boiling helium bath. Helium boils off at 1.3 L/hr. The vapor-cooled current lead is used to pass the 350 A excitation current. The magnetic field strength was measured at room temperature using a Hall probe and a stretched wire system. The magnet was tested successfully to 308 A, at which the central field exceeded 6.5 T, and the peak field on coil was 8.2 T. The design and construction of the magnet and the cryostat, the quenching protection, and field measurement results will be presented and discussed.

Index Terms—Cryostat, magnetic field measurement, protection diode, vapor-cooled current lead, wavelength shifter.

I. INTRODUCTION

SUPERCONDUCTING technology has been applied for a synchrotron radiation facility to enhance the photon flux up to X-ray. For example, a superconducting wiggler with 3.5 T was installed on VEPP3 [1] in 1979 and a superconducting undulator was also installed on the ACO storage ring in 1979 at Orsay. A 5 T superconducting wavelength shifter has been operated at SRS [2] in 1983, a 4–5 T wavelength shifter operated at ESRF [3] in 1994 and a cryogen-free superconducting wavelength shifter with 5.5 T at NSRRC [4] in 2002. Recently, superconducting multipole wiggler had been constructed and operated at MAX laboratory [5] in 2003 and NSRRC [6] in 2004. Meanwhile, superconducting undulators have also been constructed and operated at ANKA [7] and the prototype construction has been done at LBNL [8] and NSRRC [9]. These superconducting insertion devices can provide the high flux X-ray for the experiments of protein crystallography, material science, and X-ray scattering. Moreover, superconducting MgB₂ wires

TABLE I
SPECIFICATIONS OF SUPERCONDUCTING WAVELENGTH SHIFTER

Number of pole	3
Physical length (cm)	85
Beam duct aperture HxV (cm)	10 (2)
LHe boiling off (L/hr)	< 2
Beam duct temperature (K)	300
Peak field (T)	6.5
Average excitation rate (A/s)	0.5
Critical energy @ 1.5 GeV (keV)	9.72
First Integral of normal (skew) terms (G-cm)	<±20
Second Integral of normal (skew) terms (G-cm ²)	<±35000 (5000)
Normal (skew) quadrupole (G)	<±25
Normal (skew) sextupole (G/cm)	<±50
Normal (skew) octupole (G/cm ²)	<±50

and high-temperature superconducting BSCCO wires have recently become commercially available. Hence, superconducting insertion devices will have the greatest potential of providing hard X-rays in the medium-energy synchrotron light source. Consequently, a superconducting wavelength shifter (SWLS) has been constructed by winding NbTi wires to meet this increasing demand of users.

The overall length of the wavelength shifter, including its cryogenic vacuum vessel, is only 600 mm. Therefore, the SWLS can be installed in a very short straight section. The magnetic circuit design and field calculations of the superconducting wavelength shifter were carried out by the Radia Code [10]. This code was also used to optimize the cross-section of the iron pole to minimize the multipole components. Since the vertical warm gap is 20 mm to meet the beam dynamics and injection efficiency requirements, the actual magnet cold gap has to be at least 50 mm to allow space for the thermal shielding and wall thickness of the aluminum warm beam duct.

Despite the limitations of the length and the large magnet gap requirement, a central pole was designed with a maximum field of 6.5 T. Consequently, the critical photon energy of 9.72 keV is obtained in a 1.5 GeV TLS or 38.9 keV in a 3 GeV TPS. A 250 liters liquid helium bath and a 15 liters liquid N₂ reservoir are included in this design for magnet cooling and thermal shielding, respectively. Table I presents the related parameters and specification of the SWLS. Two vapor-cooled current leads are employed to reduce the leaking of heat to the 4.2 K components. A gas-electrode insulation array is used to pass the main current and recover the warm helium gas. Two pairs of back-to-back cold diodes are used for quench protection. Eight suspensions were adopted to fix the magnet in the 300 K vessel.

The results of magnet testing demonstrate that a nominal field of 6.5 T at an excitation current of 304.8 A was obtained in twice training in the vertical test dewar. The real boil-off rates of

Manuscript received August 28, 2006. This work was supported in part by the National Science Council of Taiwan under Contract NSC 95-2112-M-213-008.

C. S. Hwang, F. Y. Lin, J. C. Jan, C. H. Chang, H. H. Chen, M. H. Huang, K. T. Hsu, and G. Y. Hsiung are with the Institute of National Synchrotron Radiation Research Center, Hsinchu 30076, Taiwan, R.O.C. (e-mail: cshwang@nsrrc.org.tw).

B. Wang, B. Wahrer, C. Taylor, C. Chen, and T. Juang are with the Wang NMR, Livermore, CA 94550 USA (e-mail: wangnmr@yahoo.com).

Color versions of one or more of the figures in this paper are available online at <http://ieeexplore.ieee.org>.

Digital Object Identifier 10.1109/TASC.2007.899830

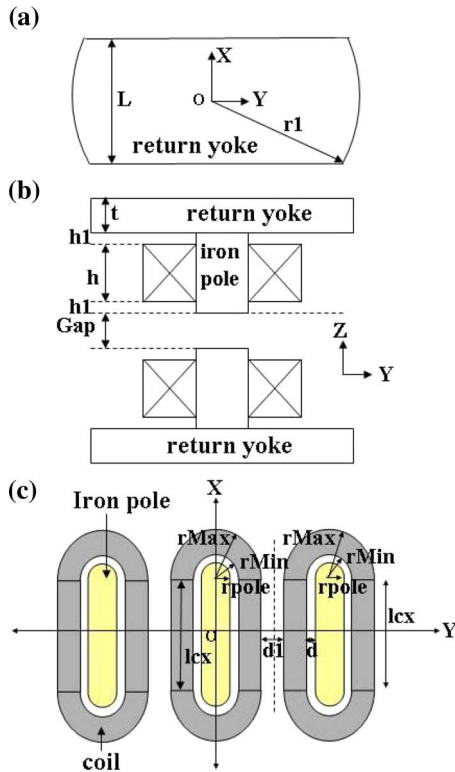


Fig. 1. Schematic design of the coil, iron pole and return yoke. The dimensions description of (a) the return yoke on the top view, (b) the return yoke, iron pole and coil on the side view, and (c) the coil and iron pole on the top view.

liquid helium and liquid nitrogen are approximately 1.3 L/hr and 0.2 L/hr, respectively. Finally, the highly accurate Hall probe and stretched wire systems [11] were employed to measure the roll-off of the central pole, and the integral multipole components along the curved and straight trajectory, respectively.

II. DESIGN AND CONSTRUCTION OF MAGNET

A. Magnet Circuit Design and Force Analysis

Fig. 1 shows the magnet circuit design, including the superconducting coils, iron poles, and flux return yoke. Material of 1006 steel was used as the magnet poles and fluxes return, to enhance the magnetic field strength. The distributions of the magnetic field and the first and second integral field along the longitudinal axis were calculated, as displayed in Fig. 2 that shows the data are in agreement on the measured and calculated field. Fig. 2(c) reveals that the synchrotron radiation source point of the central pole is offset 8.73 mm away from the magnet center. The downstream vacuum chamber should be offset 8.73 mm from the magnet center to prevent the synchrotron radiation heating the downstream chamber. Fig. 3 shows the magnetic field roll-off, $\Delta B/B$, of the central and side poles. The roll-off $\Delta B/B \geq 0.1\%$ at the central pole is ± 15 mm. A wider integral good field region can be obtained by increasing the length lc_x of the side poles in the transverse direction, as shown in Fig. 4. After the length lc_x was optimized, the multipole components, especially the integral sextupole field strength (calculated along the straight trajectory), are adjusted close to zero.

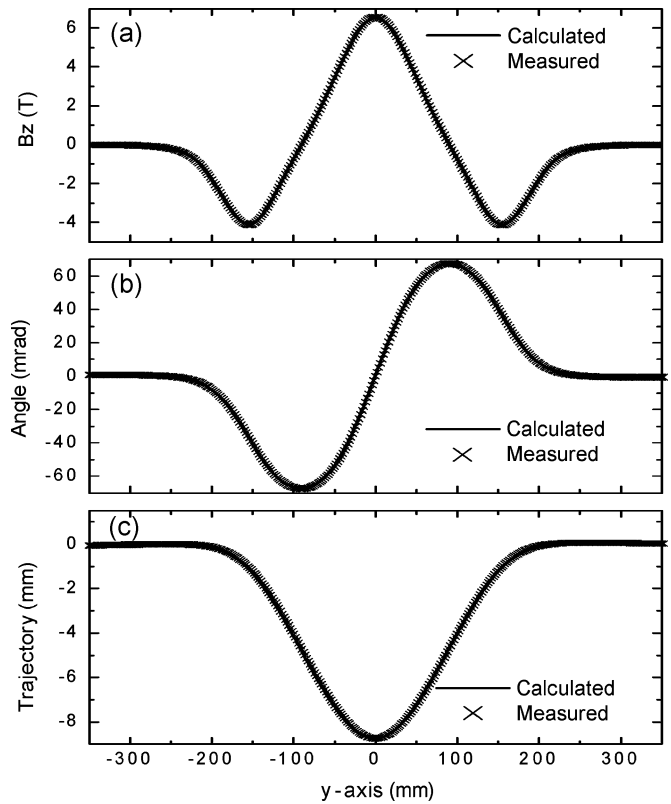


Fig. 2. Distribution of (a) magnetic field, (b) first integral field, and (c) second integral field, along the longitudinal axis. The solid and cross line plot the calculated and measured results, respectively (calculated at 1.5 GeV).

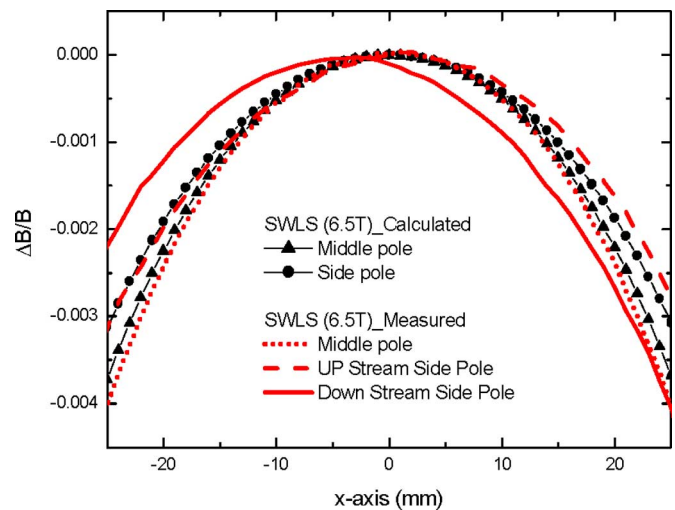


Fig. 3. Calculated and measured field homogeneity ($\Delta B(x)/B(0)$) of the three poles on the transverse x-axis.

Table II presents the optimized dimensions of the magnet circuit. However, the electron orbit at the center of the magnet has an offset of 8.73 mm (Fig. 2(c)) that will create a quadrupole field strength (Fig. 4) if the field is integrated along the true electron beam trajectory (calculated along the curved trajectory). At a central field of 6.5 T, most of the pole tip is saturated. However, the cross-section of the yoke through which the fluxes return is large enough to avoid saturation near the outside boundaries in

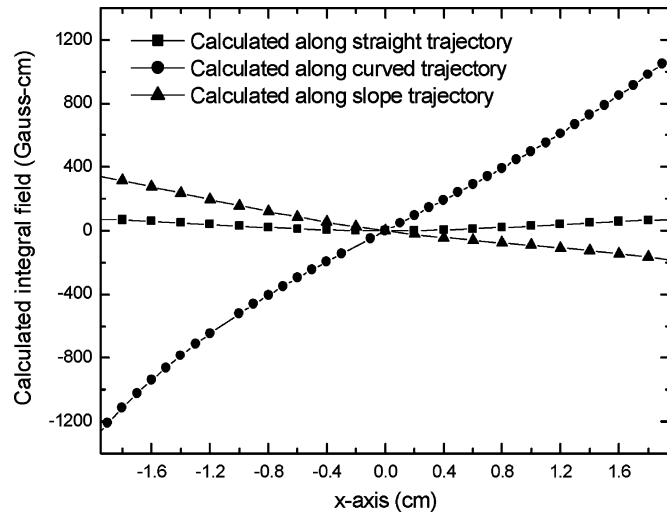


Fig. 4. Calculated integral field distribution $\int B(x)dy$ along the straight, curved and slope trajectories on the transverse x-axis.

TABLE II
DIMENSIONS OF THE MAGNET CIRCUIT DESIGN

Gap (mm)	50	
h (mm)	70.776	
h1 = d (mm)	1.4	
d1 (mm)	14.999	
t (mm)	152.4	
r1 (mm)	249	
L (mm)	200	
	Middle Poles	Side Pole
rMax (mm)	83.294	56.207
rMin (mm)	20.48	12.9
rpole (mm)	19.08	11.5
lcx (mm)	139	174
Coil Cross-section (mm)	62.81×70.78	43.31×70.78
No. of turns	58×36	40×36
Current density J_0 (A/mm ²)	145.5	145.5
Operation current I_0 (A)	307.8	307.8

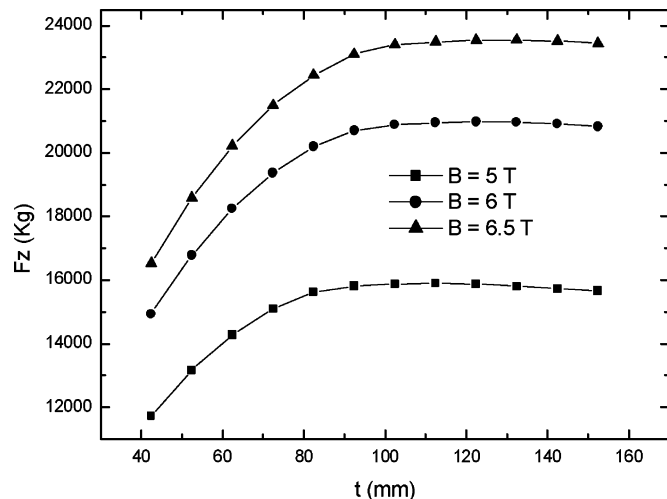


Fig. 5. Calculated force between return yoke and coil vs. the thickness of the return yoke in different central field strength.

TABLE III
SUPERCONDUCTOR SPECIFICATION

Bo (Bs) @ center pole (T)	6.5 (8.2)
Bo (Bs) @ side pole (T)	-4.1 (6.2)
Cu/Sc ratio	3:1
Number of Filament	330
Wire diameter with insulated (mm ²)	1×1.9
Construction diameter (mm ²)	1.083×1.966
Critical current @ 8 T (A)	428
Critical current Density @ 8 T (A/mm ²)	1221
RRR	200
Twist pitch (mm)	26
Filament diameter (μm)	39
Inductance @ 6.5 T (H)	9.53
Total energy @ 6.5 T (kJ)	450

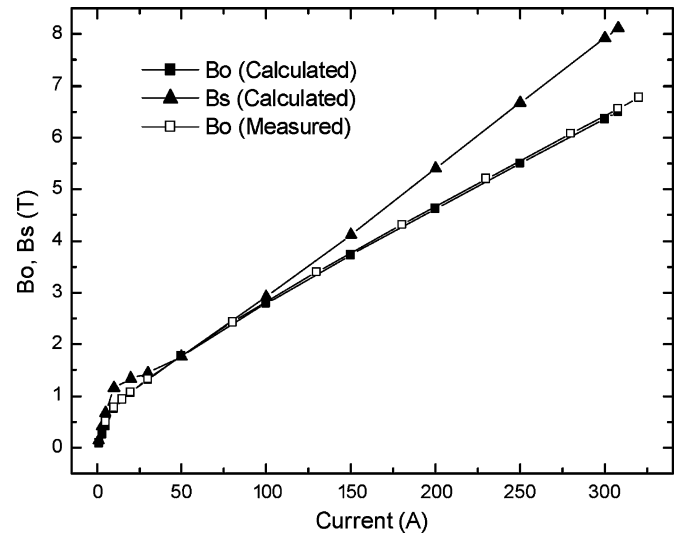


Fig. 6. Peak field B_0 at center position and the peak field B_s on superconducting coil at different excitation currents.

order to minimize the stray fields. Fig. 5 displays the relationship between the thickness of the return yoke and the force between the coil and the return yoke, indicating that the thickness, 152.4 mm, is enough to prevent the field saturation.

Table III presents the main design parameters and the specifications of the conductor. A rectangular NbTi superconductor was chosen because of its high packing factor. The critical current I_c of the conductor is 428 A at $B_s = 8$ T. The peak fields B_s in the coil is 8.2 T when the central pole field B_0 is 6.5 T, as shown in Fig. 6. After pole optimization, the ratio B_s/B_0 is 1.26. The design operation current $I_0 = 307.8$ A is 73% of the critical current I_c . For the conductor stress analysis, each coil is divided into four segments—two straight and two curved (see Fig. 1). In the z direction, all coils are compressed against its iron yoke. In both the x and the y directions, the coil expansion (hoop) forces are large. However, the coil ends (curve segment) are designed to be self-supporting, so the mean tensile stress is 3356 psi for the central coil and 1769 psi for the side coils. In the y direction, an aluminum block supports the forces and the shear stresses of the middle and side coils are 4324 psi and 6020 psi, respectively. In this case, the mean compressive stress of the central coil straight segment reaches 4537 psi and that for the side coil is 2505 psi. Therefore, the aluminum block will provide tight support for the coil after cooling. Fig. 7 plots the inductance

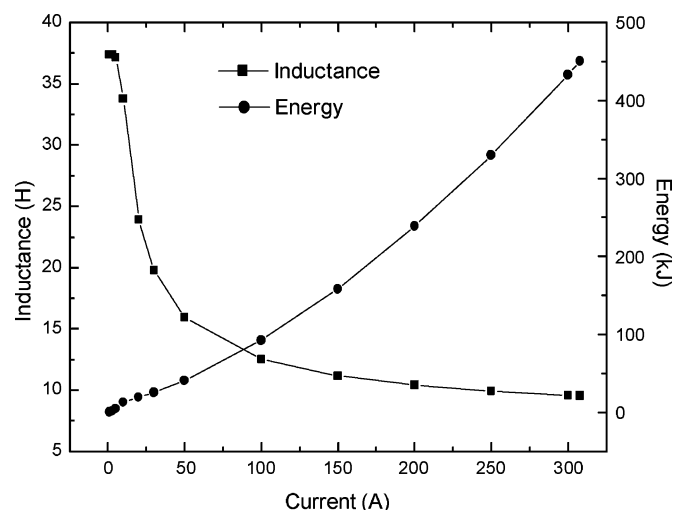


Fig. 7. Calculated inductance and energy as function of excitation current.

and energy as functions of the excitation. This data is very important for determining the specification of power supply and designing the quenching protection circuit.

B. Cryostat Design and Construction

A liquid helium bath cryostat with a residual of 125 L volume above the top of the magnet is used for cooling magnet and a 15 L liquid nitrogen reservoir is for radiation shielding and conduction thermal intercept. Reservoirs of the liquid helium and nitrogen are made of stainless steel and aluminum, respectively. Fig. 8 presents the magnet cryostat and mechanical design of the superconducting wavelength shifter. An adjustable support structure was designed for the pitch, yaw, row, and the positioning of the three axes to perform an accurate alignment.

On the upper half of the cryostat, two pairs of penetration stainless steel tubes (one with an OD of 0.05" and the other with an OD of 0.035") are welded to the helium and the nitrogen reservoirs, respectively. These tubes are for inserting a liquid level probe, transferring liquid, venting gas and installing a safety valve, a burst disk and a pressure gauge. An extra tube is inserted in the helium reservoir for returning the cold gas. The safety valve, the burst disk and the pressure gauge are also installed in the helium service tower. The heat flow from the tubes is intercepted by the liquid nitrogen. Fig. 9 shows the cross-section of the cryostat aperture through which is inserted the aluminum vacuum chamber. The warm bore is vacuum-sealed by an extruded beam duct made of 6063 aluminum with a thickness of 4.25 mm. The inner cross-section $100 \times 20 \text{ mm}^2$ of the beam duct is equipped with a hot water channel for vacuum baking. There are four window ports with 4" flange for the magnet alignment.

Most of the heat leaked to 4 K components is through the main power current leads. Table IV presents an estimate of the cryostat heat load. This table reveals that the liquid helium and nitrogen consumption rate are 1.47 L/hr and 0.2 L/hr, respectively. The power current cryogenic-ceramic feedthrough is CERMASEAL NW16CF conflict flange (8 kV, 330 A) that was connected with the vapor-cooled current leads (0.1 V, 350 A) through the gas-electrode insulation array. This array is used to pass both of the main excitation current and the recirculation cold helium gas. The gas-electrode insulation array consists of

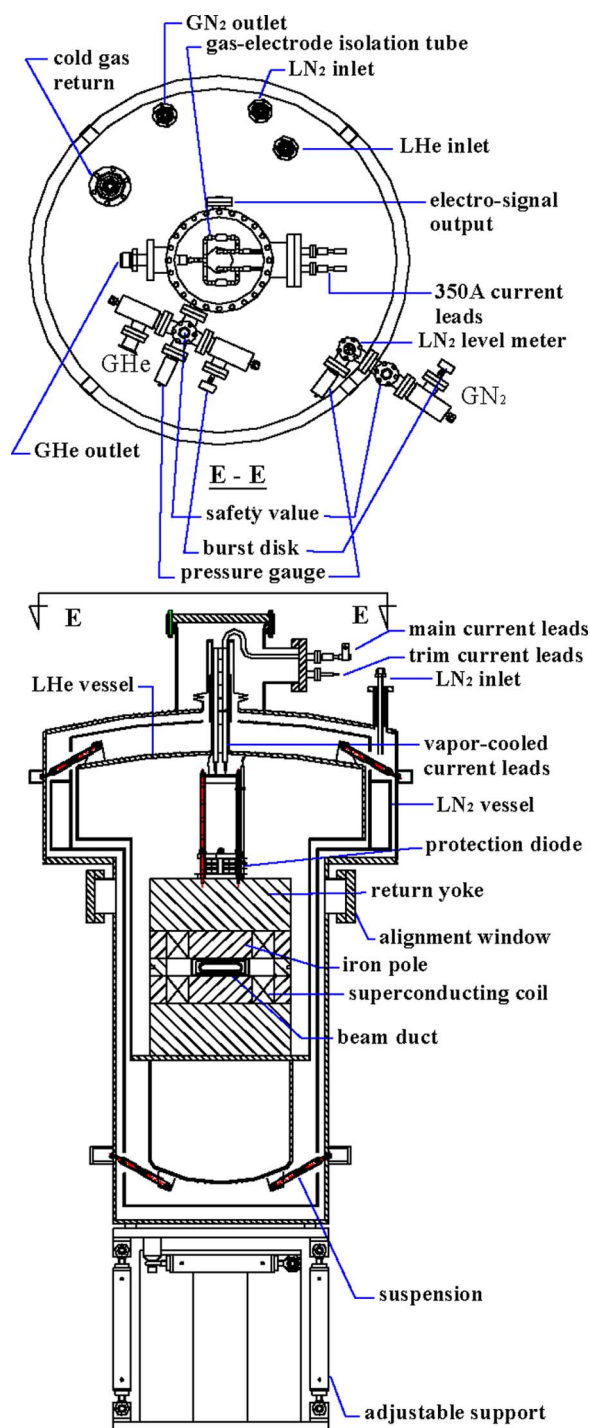


Fig. 8. Mechanical structure of main part of magnet: top view (upper drawing) and side view (lower drawing).

CERMASEAL cryogenic-ceramic isolators (13 kV, ID 0.25") and the copper tube. The annular space between the radiation screen and the outer vacuum vessel is filled with many layers of the aluminized Mylar insulation. Therefore, a minimum space of 9.5 mm is left for the radiation screen. However, a space of only 3 mm exists between the 300 K beam duct and the 77 K shielding copper (with a thickness of 1 mm). Fig. 9 shows the cross-section dimensions of the 4.2 K, 77 K, and 300 K aperture. A 3.5 mm-thick of 4.2 K duct was used to resist the 60 psi pressure difference.

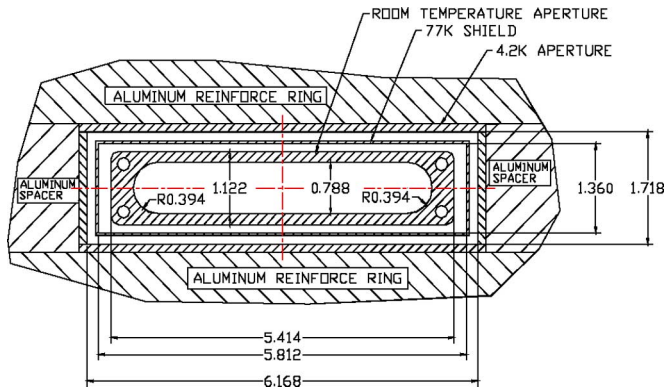


Fig. 9. Dimensions of designed cross-section apertures of the 4.2 K vessel duct, the 77 K copper shielding, and the aluminum beam duct (unit: inch).

TABLE IV
ESTIMATED CRYOSTAT HEAT LOAD

Heat leak to 4 K system- Total 1.09 W	
Cold mass suspension	0.04 W
Penetration tube	0.05 W
Vapor cool lead	0.80 W
Trim current lead	0.1 W
Radiation from thermal shield	0.1 W
Heat leak to thermal shield 77 K system- Total 8.05 W	
Suspension	0.52 W
Thermal radiation	3.88 W
Penetration tube	3.65 W

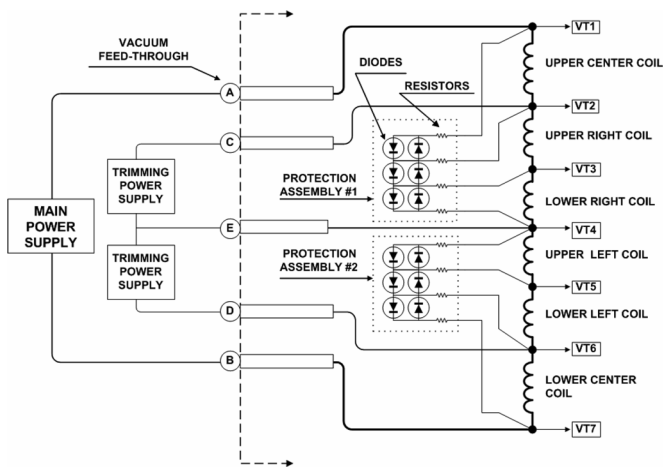


Fig. 10. Electronic circuit layout of the power current lead and the quench protection circuit.

C. Quench Protection Algorithm

Fig. 10 shows the circuit layout of the power current leads and the quench protection. Three power supplies are needed to charge and discharge the magnet. One main power supply with an output of 350 A and 10 V is connected in series with all six coils to generate the nominal peak field. Hence, one pair of vapor-cooled leads through which is passed 350 A is connected between the superconducting wire at 4.2 K and the normal copper current leads at room temperature. Additionally, two trim power supplies, each with an output of 15 V and ± 10 A, are connected in series to the two side coils, respectively, to nullify the first and second field integrals.

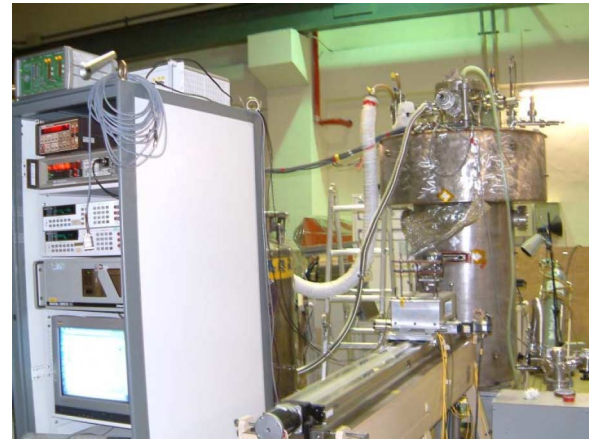


Fig. 11. Photograph of the SWLS magnet and the Hall probe measurement system.

If quenching occurs on the superconducting coil, the quenching-protection circuit is utilized to reduce the coil voltage and the coil temperature, and to minimize the induced current. Two pairs of back-to-back R620 cold diodes with 5 m Ω stainless steel resistors. Each pair of back-to-back diode arrays is connected across the three coils to form the hardware quench-protection circuit that is active when the voltage across any coil is over 4 V. The resistors in series with the diodes help to dissipate the stored energy and limit the build-up of current in the other coils. Any quenching of the magnet is detected by comparing the differential voltage between the two protection circuits. Additionally, when the cross-voltage at the two terminals of the vapor-cooled current leads exceeds 0.1 V, a warning signal will be sent to the control system and to turn off the power supply.

III. CONSTRUCTION AND ASSEMBLY OF MAGNET

Since the magnet is cooled by pool boiling, the coil bobbin is made of 1 mm thick OFHC-copper (see Fig. 1). The bobbin is insulated in three layers of Kapton with high thermal conductivity. Each coil is individually wound on a winding fixture, which defines the axial length and the coil height. Based on the force analysis, an aluminum support structure was used to reinforce of the pole and the coil. Hence, two aluminum blocks are impregnated with poles and coils in each up and down magnet array, respectively. The mechanical structure of the conductor coil and the cold mass assembly provide mechanical support to the large forces generated by the pole coil. The completed coil fits to the iron pole and the aluminum-supporting block. The 1.4 mm gap between the coils and the aluminum block is filled with epoxy to reinforce and glue the coil onto the aluminum block. The return yoke together with the iron poles were carefully aligned, pinned and bolted together with high precision. The aluminum block not only supports for both the in-plane and the out-of-plane coil forces but also takes care of the thermal contraction of the coils. It was bolted to the return yoke. A magnet gap separator made of aluminum bars maintains a gap of exactly 50 mm between the up and down magnetic arrays. The upper and lower iron yokes are then bolted to the aluminum block to compress the coils against the aluminum block. Four survey targets on the return yoke are used in the alignment of the magnet. Fig. 11 reveals the photograph of the magnet system with the Hall probe magnet field measurement system.

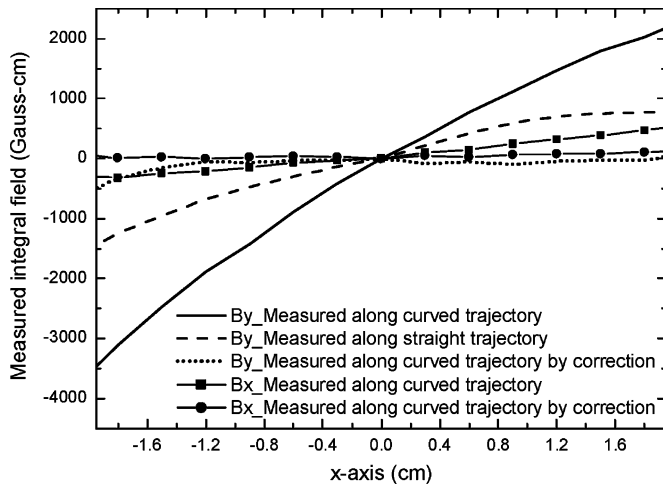


Fig. 12. Measured integral field ($\int B(x)dy$) distribution along different trajectory on the transverse x-axis.



Fig. 13. Two magic-finger correctors were installed in SWLS both sides. Arrow indicates the magnetic field direction of the normal corrector.

IV. TESTING MAGNET PERFORMANCE

Twice training yields the current of 308 A in the vertical test dewar. However, when the magnet was assembled with the magnet cryostat and re-charged, the nominal field of 6.5 T was easily obtained without training. The measured consumption rates of liquid helium and nitrogen was 1.3 L/hr and 0.2 L/hr, similar to the estimated heat loads. A room-temperature Hall probe and stretched wire were used to measure the field distribution of the magnet. Fig. 12 presents the distributions of the field integrals along the straight and curved trajectories. The trim current upstream and downstream of the both end poles was excited by 4.8 A and 3.9 A to correct the first and second integral fields, respectively. Fig. 6 plots the calculated and measured field strength vs. the current. The difference of the field strength between the calculated and measured field is about 1%. Fig. 3 shows the measured magnetic field roll-off, $\Delta B/B$, revealing a 3.5 (0.5) mm offset of the center of downstream (upstream) side pole that are relative to central pole.

An integral field along the slope line (the slope line was defined by the two center offsets) was calculated and revealed in Fig. 4. These two offsets induce higher integral multipole components. However, the real integral field should be integrated along the true electron beam orbit (measured along curved trajectory). The measured integral field (Fig. 12) reveals an integral quadrupole field that is similar to the field calculated along the curved trajectory (Fig. 4). Therefore, two magic-finger cor-

rector magnets (Fig. 13) are required at each ends of the magnet to correct the quadrupole field strength (one for the normal component and the other for skew component). The measured integral quadrupole field strength (Fig. 12) was then compensated to be within the specification (Table I) by exciting 10 A on the normal (skew) magic-finger corrector.

V. CONCLUSION

This wavelength shifter magnet can be charged to nominal field without training when the magnet cools again. The gas-electrode insulation array design is used to prevent power current ceramic-feedthrough freezing. It is necessary to calculate the integral field along the true electron beam orbit on designing the strong field of a wavelength shifter. The magic-finger corrector magnet can be used to correct the normal and skew integral multipole field strength. Care must be taken to prevent the synchrotron radiation of wavelength shift itself heating the downstream chamber.

ACKNOWLEDGMENT

The authors thank the colleague of NSRRC, especially Dr. C. T. Chen, K. S. Liang and J. R. Chen to support this project. The authors also thank the staffs of NSRRC, D. J. Wang, Jenny Chen, K. H. Hu, Y. C. Chien, C. C. Chang, W. P. Le and P. H. Lin for their technical assistance.

REFERENCES

- [1] A. S. Artamonov, L. M. Barkov, V. B. Baryshev, N. S. Bashtovoy, N. A. Vinokurov, E. S. Gluskin, G. A. Kornukhin, V. A. Kochubei, G. N. Kulipanov, N. A. Mezentshev, V. F. Pindiurin, and A. N. Skrinsky and V. M. Khorev, "First results of the work with a superconducting "snake" at the VEPP-3 storage ring," *Nucl. Instr. Meth.*, vol. 177, pp. 239–246, 1980.
- [2] V. P. Suller, N. Marks, M. W. Poole, and R. P. Walker, "SRS behaviour with a superconducting 5-Tesla wiggler insertion," *IEEE Trans. Nucl. Sci.*, vol. NS-30, no. 4, pp. 3127–3129, 1983.
- [3] H. H. J. Ten Kate, D. Ter Avest, A. Ravex, M. Lagnier, and P. Elleaume, "re-design study of a 4–5 T superconducting wiggler magnet for the ESRF," *IEEE Trans. Magn.*, vol. 30, no. 4, pp. 2543–2546, 1994.
- [4] C. S. Hwang, B. Wang, R. Wahrer, H. H. Chen, C. H. Chang, F. Y. Lin, T. C. Fan, and C. T. Chen, "Construction and performance of a compact cryogen-free superconducting wavelength shifter," *IEEE Trans. Appl. Supercond.*, vol. 12, no. 1, pp. 686–690, 2002.
- [5] E. wallen, G. LeBlanc, and M. Eriksson, "The MAX-wiggler, a cold bore superconducting wiggler with 47 3.5 T poles," *Nucl. Instrum. Meth. A*, vol. 467, pp. 118–120, 2001.
- [6] C. S. Hwang, C. H. Chang, H. H. Chen, F. Y. Lin, T. C. Fan, M. H. Huang, J. C. Jan, K. T. Hsu, J. Chen, S. N. Hsu, G. Y. Hsiung, H. P. Chang, C. C. Kuo, Y. C. Chien, F. Z. Hsiao, J. R. Chen, and C. T. Chen, "Superconducting wiggler with semi-cold beam duct at Taiwan light source," *Nucl. Instrum. Meth. A*, vol. 556, pp. 607–615, 2006.
- [7] S. Casalbuoni, M. Hagelstein, B. Kostka, and R. Rossmanith, "Generation of x-ray in a storage ring by a superconductive cold-bore in-vacuum undulator," *Phys. Rev. ST Accel. Beams*, vol. 9, p. 010702, 2006.
- [8] S. O. Prestemon, D. R. Dietderich, S. E. Bartlett, M. Coleman, S. A. Gourlay, A. F. Lietzke, S. Marks, S. Mattafirri, R. M. Scanlan, R. D. Schlueter, B. Wahrer, and B. Wang, "Design, fabrication, and test results of undulators using Nb3Sn superconductor," *IEEE Trans. Appl. Supercond.*, vol. 15, no. 2, pp. 1236–1239, 2005.
- [9] C. S. Hwang, J. C. Jan, P. H. Lin, C. H. Chang, M. H. Huang, F. Y. Lin, T. C. Fan, and H. H. Chen, "Mini-pole superconducting undulator for X-ray synchrotron light source," *IEEE Trans. Appl. Supercond.*, vol. 16, no. 2, pp. 1855–1858, 2006.
- [10] P. Elleaume, O. Chubar, and J. Chavanne, "Computing 3D magnetic field from insertion devices," in *PAC1997*, Vancouver, Canada, 1997, pp. 3509–3511.
- [11] C. S. Hwang, F. Y. Lin, and T. C. Fan, "Integral magnetic field measurement using an automatic fast long-loop-flip coil system," *IEEE Trans. Instrum. and Meas.*, vol. 52, no. 3, pp. 865–870, 2003.